A NOVEL HIGH-PRECISION OBSERVATION MODE FOR THE TRACKING AND IMAGING RADAR TIRA - PRINCIPLE AND PERFORMANCE EVALUATION

D. Cerutti-Maori, J. Rosebrock, C. Carloni, M. Budoni, I. Maouloud, and J. Klare

Fraunhofer Institute for High Frequency Physics and Radar Techniques FHR, Fraunhoferstrasse 20, 53343 Wachtberg, Germany, Email: Delphine.Cerutti-Maori@fraunhofer.fhr.de

ABSTRACT

This paper presents a high-precision observation mode for the Tracking and Imaging Radar TIRA, which is currently under development. After introducing the principle of this new experimental mode, the paper examines its applicability depending on the orbital parameters on the basis of simulations. Several data collections were performed to calibrate the new mode. Accurate ephemerides were used to compute the residuals of the different observables and assess experimentally the performance of this mode. Results of the calibration measurements are shown in this paper as well as a statistical analysis of the residuals. It could be demonstrated that the estimation accuracy could be improved for all the measured parameters. Finally, some applications of this new experimental mode are discussed.

Keywords: Radar for space observation; Observation mode; Radar observables.

1. INTRODUCTION

With the increasing number of resident space objects, ensuring the security in space becomes more important than ever. Space observation systems such as optical sensors, radar systems, and SLR (Satellite Laser Ranging) systems play an important role by providing accurate orbit measurements. For instance, high-precision orbital data are required to compute potential collision probabilities between space objects, re-entry windows of a decaying object, preliminary orbits during mission starts, or for updating space object catalogues.

Radar systems for space observation are active systems operating at microwave frequencies. A major advantage of radar systems over optical systems is that they can observe space objects at any time a day in all-weather conditions. In addition, radar systems are particularly adapted for uncontrolled objects after system failure and for non-cooperative space objects, which do not carry any retro-reflectors. This makes them more versatile compared to SLR systems. However, they are not as accurate as SLR systems. The Tracking and Imaging Radar TIRA [1], developed and operated at Fraunhofer FHR, combines a tracking radar and an imaging radar with an agile 34 m reflector antenna. This large reflector is the core component of the TIRA system. The resulting high antenna gain enables the imaging of LEO (Low Earth Orbit) satellites with a high radiometric resolution. In addition, small space objects can be reliably detected and their parameters accurately estimated. So far, only the data of the tracking radar were used to generate the tracking data delivered to our partners.

Following an internal goal to deliver data with improved accuracy to better support the demand of space agencies and of the GSSAC (German Space Situational Awareness Centre), an experimental high-precision observation mode for TIRA is currently under development. This new observation mode uses the data measured by both radars in order to improve the accuracy of the measured parameters. The paper is organised as follows. Section 2 introduces the principle of the new experimental mode. A derivation of the signal processing developed for the two radars is given in Section 3. Section 4 presents the results of a statistical investigation that was conducted to evaluate the applicability of the new experimental mode. Several calibration measurements were performed to assess the performance of the new processing mode, which are shown in Section 5. Different applications are addressed in Section 6. Finally, Section 7 concludes the investigation.

2. PRINCIPLE OF THE HIGH-PRECISION OBSERVATION MODE

As mentioned in the previous section, the TIRA system combines two radars: a tracking radar operating in L-band with a center frequency of 1.3 GHz and an imaging radar operating in Ku-band with a center frequency of 16.7 GHz. Both radars are coherent pulse radars. The L-band radar is equipped with a monopulse system for real-time tracking and controls the Ku-band radar.

Until now, solely the L-band radar was used to generate measurement vectors from the observation of a space object. These observation vectors include the measurement

of the space object range, range rate, azimuth and elevation angles, and radar cross section at different instants of time. In order to increase the estimation accuracy of the different observables, the high-precision observation mode utilizes both radars when performing an observation and fuses the information contained in the data acquired by the two radars. The observation vectors are delivered in the CCSDS/TDM (Consultive Committee for Space Data Systems / Tracking Data Message) format [2].

An innovative processing of the tracking radar data was developed, which consists of several consecutive processing steps. This processing allows for the estimation of a new parameter, the range rate rate. In a first step, an initial estimate of the range rate and of the range rate rate is gained through a weighted LS (Least Square) over N observations vectors. These initial estimates are then refined in a second step through a coherent processing. The usual PRF (Pulse Repetition Frequency) of the TIRA system is 30 Hz. Caused by the existing very high range rates $\dot{R}$ of several km/s between TIRA and the space objects, the occurring Doppler frequencies $f_d = -\frac{8.9}{[\mathrm{m}]}\dot{R}$ can be in the order of several tens of kHz. Doppler frequencies estimated over several pulses may be ambiguous. The goal of the third processing step is to resolve potential range rate ambiguities that could appear for the filtered range rate. In a last processing step, the estimation accuracy of the remaining observables can be improved through a weighted LS filter.

A second measurement of the range of space objects can be obtained with the imaging radar. Since the bandwidth of the imaging radar is much larger compared to the one of the tracking radar, a much more precise measurement of the range can be obtained by processing the imaging radar data. A dedicated signal processing was developed to extract the absolute range of the objects from the range profiles. This processing resolves the range/Doppler ambiguities that exist for linear frequency modulated waveforms.

3. RADAR SIGNAL PROCESSING

This section presents the signal processing developed to process the data acquired by the tracking radar and the imaging radar. For the sake of clarity, this section is separated from the previous part of the paper as a stand alone section.

3.1. Signal processing for the tracking radar

The processing technique introduced in this section can be applied to any coherent radar system. Radar systems equipped with several receive channels such as the TIRA system or the GESTRA (German Experimental Space Surveillance and Tracking Radar) system [3, 4] can measure additionally the azimuth and elevation angles of a space object for each radar pulse. While the TIRA system uses a parabolic reflector antenna together with a monopulse system, the GESTRA system utilizes a multichannel phased-array antenna in combination with digital beamforming to measure these angles.

Consider a space object, which can be modelled as a single point scatterer. This assumption is fulfilled by the tracking radar of the TIRA system since the object dimension is small compared to a radar range/Doppler resolution cell. Let $R(t)$, $\dot{R}(t)$, $\ddot{R}(t)$, $\theta(t)$, and $\varphi(t)$ be the true range, the true range rate, the true range rate rate, the true elevation angle and the true azimuth angle of the observed space object at epoch t, respectively.

The corresponding values measured by the radar are denoted by $\hat{R}(t)$, $\hat{\dot{R}}(t)$, $\hat{\theta}(t)$, and $\hat{\varphi}(t)$, respectively, where the superscript $\hat{}$ indicates an estimated value. All these parameters can be regrouped in the observation vector $\boldsymbol{\vartheta}(t)$, together with their corresponding estimation accuracy. These different estimation accuracies are inversely proportional to the square root of the SNR (Signal-to-Noise Ratio) of the received signal and can thus be derived from the SNR [5, 6].

Coherent radars measure for each pulse and range cell an additional parameter, the complex amplitude $\hat{A}(t)$, which can be exploited to derive additional information about the space object. These complex amplitudes are the key for radar imaging such as SAR (Synthetic Aperture Radar) and ISAR (Inverse SAR). The complex amplitude for the range cell of interest can be modelled according to

$$\hat{A}(T) = |A(T)|e^{-j\frac{4\pi}{\lambda_0}R(T)} + n(T). \tag{1}$$

It corresponds to the signal reflected by the space object and received by the radar after demodulation and range compression at pulse T. In the previous equation, λ_0 is the wavelength corresponding to the carrier frequency f_0 of the tracking radar. Note that the used radar waveform should be Doppler intolerant in order to estimate the intra-pulse Doppler frequency yielding the range rate estimate. The amplitude $|A(T)|$ depends on the radar and antenna parameters (such as transmit power, transmit gain, receive gain), on the geometry (e.g. range, position of the object in the antenna beam), on the occurring losses (e.g. propagation losses), and on the object characteristics (RCS (Radar Cross Section)) [6]. The noise signal $n(T)$ is modelled as a WGN (White Gaussian Noise).

The radar transmits regularly pulses at the rate specified by the PRF. The measured complex amplitudes over N pulses can be regrouped in the measurement vector $\mathbf{z}$ for further processing

$$\mathbf{z} = \begin{bmatrix} \hat{A}(T_1) \\ \hat{A}(T_2) \\ \vdots \\ \hat{A}(T_N) \end{bmatrix}. \tag{2}$$

The processing developed to improve the estimation accuracy of the measured range and range rate and to determine the range rate rate parameter assumes a quadratic range history over these N pulses. This is an usual assumption used by SAR systems (see for example the derivation of the range/Doppler processor [7]). This assumption is also employed for detecting moving objects with multi-channel radars [8]. Let's approximate the range $R(T)$ by a second order Taylor approximation around the time T_c chosen in the middle of the considered time interval. The range between the radar and the satellite can be written as

$$R(T) \approx \tilde{R}_{T_c} + \tilde{\dot{R}}_{T_c}(T - T_c) + \frac{1}{2}\tilde{\ddot{R}}_{T_c}(T - T_c)^2, \quad (3)$$

where the range, range rate, and range rate rate are denoted by $\tilde{R}_{T_c}$, $\tilde{\dot{R}}_{T_c}$, $\tilde{\ddot{R}}_{T_c}$, respectively.

As already mentioned in the previous sections, the processing combines successive estimation steps. During the first estimation step, an initial estimate of the range rate $\tilde{\dot{R}}_{T_c}$ and of the range rate rate $\tilde{\ddot{R}}_{T_c}$ is gained through a weighted LS over N observation vectors $\boldsymbol{\vartheta}(T)$. After estimating these initial parameters denoted by $\widehat{\dot{R}}_{T_c}$ and $\widehat{\ddot{R}}_{T_c}$, respectively, a phase correction

$$\mathbf{Q} = \text{diag}\begin{bmatrix} e^{-j\frac{4\pi}{\lambda_0}\widehat{\dot{R}}_{T_c}(T1-T_c)}e^{-j\frac{2\pi}{\lambda_0}\widehat{\ddot{R}}_{T_c}(T1-T_c)^2} \\ e^{-j\frac{4\pi}{\lambda_0}\widehat{\dot{R}}_{T_c}(T2-T_c)}e^{-j\frac{2\pi}{\lambda_0}\widehat{\ddot{R}}_{T_c}(T2-T_c)^2} \\ \vdots \\ e^{-j\frac{4\pi}{\lambda_0}\widehat{\dot{R}}_{T_c}(T_N-T_c)}e^{-j\frac{2\pi}{\lambda_0}\widehat{\ddot{R}}_{T_c}(T_N-T_c)^2} \end{bmatrix} \quad (4)$$

can be applied to the vector $\mathbf{z}$ to correct the motion of the object. Let's define the beamforming vector

$$\mathbf{b} = \begin{bmatrix} e^{-j\frac{4\pi}{\lambda_0}\widehat{\delta\dot{R}}_{T_c}(T_1-T_c)}e^{-j\frac{2\pi}{\lambda_0}\widehat{\delta\ddot{R}}_{T_c}(T_1-T_c)^2} \\ e^{-j\frac{4\pi}{\lambda_0}\widehat{\delta\dot{R}}_{T_c}(T_2-T_c)}e^{-j\frac{2\pi}{\lambda_0}\widehat{\delta\ddot{R}}_{T_c}(T_2-T_c)^2} \\ \vdots \\ e^{-j2\frac{4\pi}{\lambda_0}\widehat{\delta\dot{R}}_{T_c}(T_N-T_c)}e^{-j\frac{2\pi}{\lambda_0}\widehat{\delta\ddot{R}}_{(}T_N-T_c)^2} \end{bmatrix}. \quad (5)$$

Through a ML (Maximum Likelihood) approach

$$[\widehat{\delta\dot{R}}_{T_c}, \widehat{\delta\ddot{R}}_{T_c}] = \text{argmax}\left\{\left|\mathbf{b}^\dagger\mathbf{Q}^{-1}\mathbf{z}\right|\right\}, \quad (6)$$

a fine estimate of the parameters $\tilde{\dot{R}}_{T_c}$, $\tilde{\ddot{R}}_{T_c}$ can be achieved. In the previous equation, the operator † denotes the complex conjugate and transpose operation. An additional processing step can be implemented that resolves the potential ambiguities that may occur for the estimated range rate $\widehat{\dot{R}}_{T_c} + \widehat{\delta\dot{R}}_{T_c}$. Similar to the first estimation step, a refined estimate of the range and of the azimuth and elevation angles can be computed through a weigthed LS.

3.2. Signal processing for the imaging radar

The imaging radar of the TIRA system uses a linear frequency modulated (chirp) signal. A major advantage of chirp waveforms is their Doppler tolerance, which simplifies the signal processing for computing radar images. TIRA uses the principle of deramping in order to generate a range profile of an object at a given time. In the following, the time-equivalent range variable r is used, which is related to the time variable $t = \frac{2r}{c}$ through the speed of light c. The factor 2 takes into account the round trip of the waves.

Let $s_{TX}(r)$ be the signal transmitted by the radar at the time-equivalent range r after modulation with the wavenumber k_0

$$s_{TX}(r) = W_s\left(r, \frac{r_s}{2}, r_s\right)e^{jk_0 r}e^{j\pi\alpha_r(r-\frac{r_s}{2})^2}. \quad (7)$$

The wavenumber $k_0 = \frac{4\pi f_0}{c}$ is proportional to the frequency f_0, which corresponds in this case to the carrier frequency of the imaging radar. The chirp rate is denoted by $\alpha_r = \frac{2}{c}\frac{B}{r_s}$, where B is the bandwidth of the transmitted signal and r_s is the pulse length. $W_s(r, r_c, r_s)$ is a real window function of length r_s centered at r_c.

Assuming a constant radial velocity of the object over the short observation time

$$R(r) = R_0 + 2\beta r \quad (8)$$

with $\beta = \frac{v_r}{c}$, the receive signal can be modelled according to

$$\begin{aligned} s_{RX}(r) &= As_{TX}\left(r - R(r)\right) \\ &= As_{TX}\left(\frac{1-\beta}{1+\beta}r - \frac{1}{1+\beta}R_0\right), \end{aligned} \quad (9)$$

where A is an amplitude term.

The deramping is achieved by multiplying the signal $s_{RX}(r)$ by the complex conjugate of the function

$$\begin{aligned} s_p(r, r_p) &= W_p\left(r, \frac{r_s}{2} + r_p, \tilde{r}_s\right)e^{jk_0(r-r_p)} \\ &\quad e^{j\pi\alpha_r(r-\frac{r_s}{2}-r_p)^2}, \end{aligned} \quad (10)$$

where r_p is the range of the replica. Deramping yields

$$s(r, r_p) = s_{RX}(r)s_p^*(r, r_p) = W(r, r_p)e^{j\phi(r,r_p)}. \quad (11)$$

The amplitude function W results from the multiplication of the two window functions W_s and W_p. The parameter $\tilde{r}_s$ in equation (10) is chosen so that W_p is guaranteed to be contained in the intersection of all possible received signals and the replica extent. Since the compressed range profile is short compared to the pulse length, the influence of W_p on the point spread function in range can be neglected.

One can show [9] that the phase function can be expressed according to

$$\phi(r, r_p) \approx \phi_0 - 4\pi\alpha_r\beta(r - r_p)^2 - 2k_0\beta(r - r_p) - 2\pi\alpha_r \left(R(\frac{r_p}{2}) - r_p\right)(r - r_p). \quad (12)$$

The first phase term ϕ_0 is common for the whole range profile. It can be neglected as it does not impact the range measurement. The second phase term $-4\pi\alpha_r\beta(r - r_p)^2$ corresponds to the residual chirp from the object motion. Since a measurement of the range rate is available from the tracking radar, this phase term can be compensated. Neglecting this term causes a defocusing of the range profile. The third phase term $-2k_0\beta(r - r_p)$ is caused by the ambiguity between range and Doppler frequency for linear modulated signals. It induces a range shift, if not corrected. As β is known, this term can be compensated. Finally, the absolute range can be extracted from the last phase term $-2\pi\alpha_r \left(R(\frac{r_p}{2}) - r_p\right)(r - r_p)$. $R(\frac{r_p}{2})$ is the searched absolute range at reflection time.

4. PERFORMANCE EVALUATION AGAINST THE ORBITAL PARAMETERS

Near-Earth space objects are orbiting the Earth on a variety of different orbit shapes and orientations and orbital planes. In order to assess wether the processing developed for the tracking radar is applicable to any of these space objects, an extensive performance analysis was performed.

The parameters of the tracking radar of the TIRA system (such as antenna beamwidth, transmit power, antenna gain) were selected for the investigation. Two different beam pointing directions were considered: a high-elevation East-staring configuration and a low-elevation South-staring configuration. The range window was chosen between 300 km and 5000 km. The software SpaceView developed at Fraunhofer FHR was used to generate a list of crossing objects with their respective parameters (range, range rate, range rate rate, azimuth and elevation angles) over the beam-crossing time. The software took as input population the full TLE (Two-Line Elements) catalogue downloaded from SpaceTrack on December 12, 2019. It propagated each object over a duration of 10 days using the simplified perturbation model SGP4. A number of 18628 objects were included in the catalogue distributed in LEO, MEO (Medium Earth Orbit), GEO (Geostationary Earth Orbit) and HEO (Highly Elliptical Orbit). The number of recorded beam crossings was 3018 for the East-staring configuration and 7013 for the South-staring one [10]. In a second step, WGN signals were generated for different SNR values and added to the noiseless parameters of the beam crossing objects, thus emulating noisy measurements. These noisy observations were then processed by the method introduced in Section 3.1.

Since the results for the East-staring and the South-staring configurations were similar, only the results for the latter configuration are presented in the following. Figure 1 shows the distributions of the crossing objects according to their inclination and eccentricity. Although the different orbital parameters are not equally represented and the number of crossing objects per bin is not always sufficient for a sound statistical investigation, it is possible to detect anomalies in the filter outputs by exploiting these beam-crossing data. Residuals between the filtered and the true range, range rate, and range rate rate are plotted against the inclination angle and the eccentricity of the space objects in Figure 2. One can see that all the distributions are uniform over the orbital parameters. No regions with larger residuals can be found. To get further insights into the filter performance, a statistical investigation of the residuals was conducted. Three different SNR values (10 dB, 20 dB, and 30 dB) were considered for the analysis.

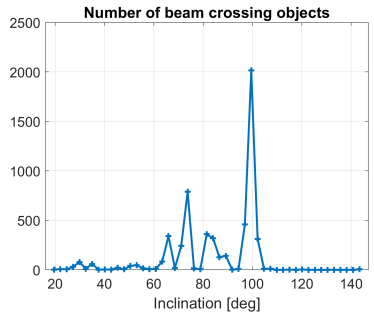

(a) Inclination

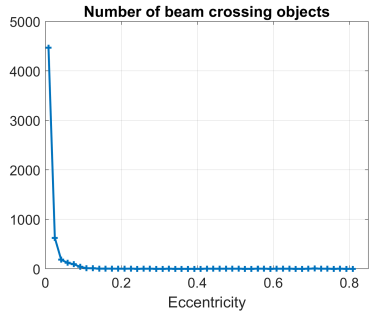

(b) Eccentricity

Figure 1. Crossing object distributions for the South-staring configuration

Figures 3 and 4 show the distributions for the elevation and azimuth angle residuals, respectively. Both angles can be estimated with an improved accuracy using a weighted LS filter. The distributions are evenly spread over the orbit inclination and the eccentricity. No bias and no filter trend can be observed over the different orbital parameters. As expected, the estimation accuracy decreases with the SNR. Note that some inclination angles and eccentricity regions are not represented because of the corresponding too small number of crossing objects.

The residual distributions for the range are shown in Figure 5. As already mentioned, the processing of the L-

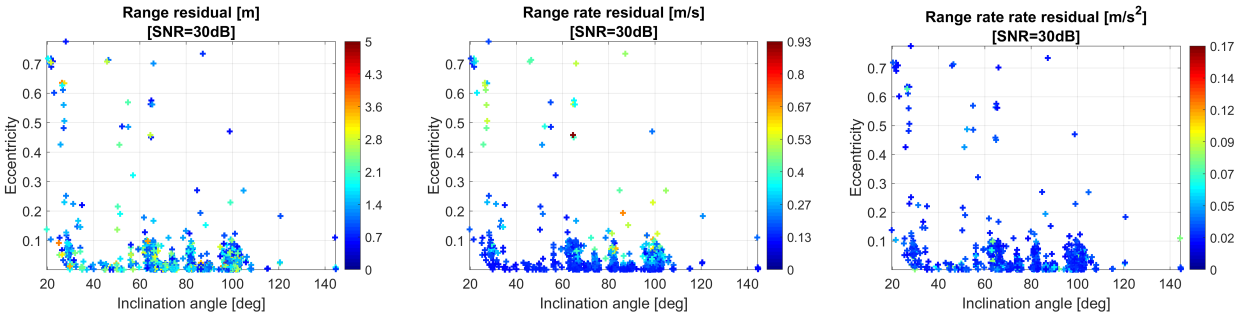

(a) Range residuals (b) Range rate residuals (c) Range rate rate residuals

Figure 2. Residuals between the estimated and the true parameters

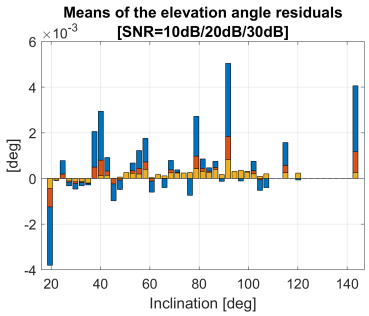

(a) Mean distribution over inclination

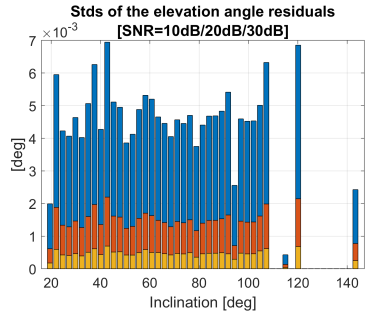

(b) Std distribution over inclination

Figure 3. Elevation angle residuals (blue: 10 dB, orange: 20 dB, yellow: 30 dB)

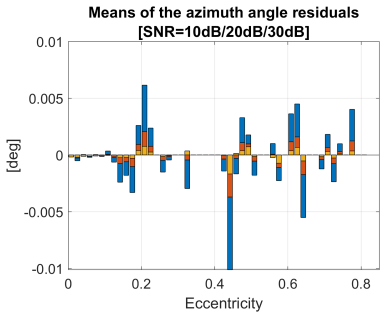

(a) Mean distribution over eccentricity

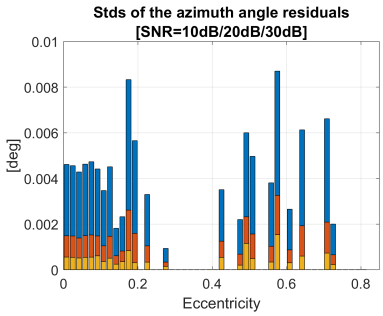

(b) Std distribution over eccentricity

Figure 4. Azimuth angle residuals (blue: 10 dB, orange: 20 dB, yellow: 30 dB)

band data assumes a quadratic range history over the considered short time interval (in the order of some seconds). If this assumption is not fulfilled, the range estimate is inaccurate. Similar to the angle distributions, one can observe that the range estimates are unbiased for the investigated inclinations and eccentricities (not shown here). The corresponding standard deviations (stds) are evenly distributed and decrease with increasing SNR values. The quality of the range estimate depends on the quality of the estimated range rate and range rate rate as well.

The estimation behaviour is similar for the range rate from a given SNR value and the range rate rate, as indicated by the residuals in Figures 6 and 7. Again, the distributions over the different orbital parameters are uniform and no orbit-dependent trend can be detected. As already explained in Section 3.1, the filter combines an initial and a fine estimation step. If the initial estimate is accurate enough, then the fine estimate will converge to the true value. This is the reason why only a slight improvement through the SNR can be achieved for the range rate (SNR$\geq$15 dB) and for the range rate rate. The issue of the range rate ambiguities caused by the low PRF is clearly visible in Figure 6 for a SNR of 10 dB. For low SNR values, it can happen that the initial estimate lies outside the unambiguous range rate interval. The final range rate estimate is thus ambiguous by a multiple of the value $\frac{PRF}{2}\frac{c}{f_0}$, which is usually around 3.4 m/s for the TIRA system. These ambiguities can be suppressed by

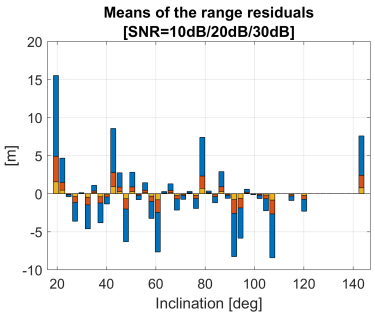

(a) Mean distribution over inclination

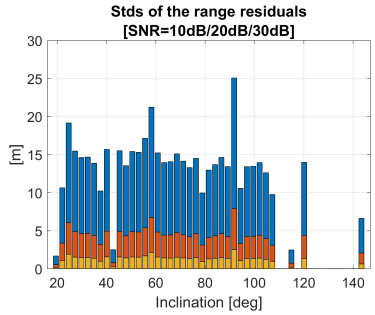

(b) Std distribution over inclination

Figure 5. Range residuals (blue: 10 dB, orange: 20 dB, yellow: 30 dB)

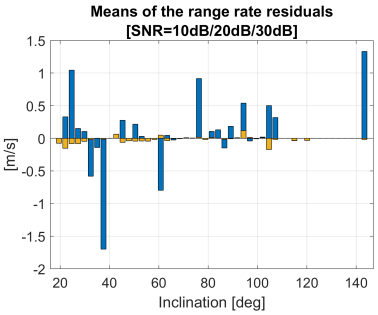

(a) Mean distribution over inclination

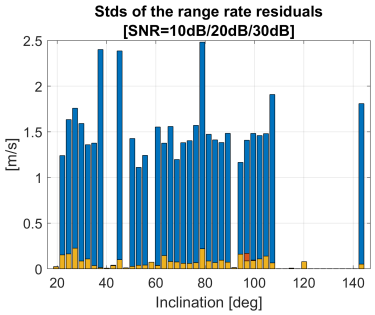

(b) Std distribution over inclination

Figure 6. Range rate residuals (blue: 10 dB, orange: 20 dB, yellow: 30 dB)

an adapted unwrapping filter.

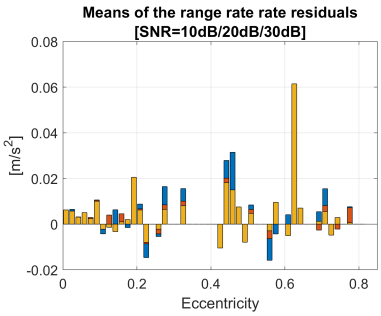

(a) Mean distribution over eccentricity

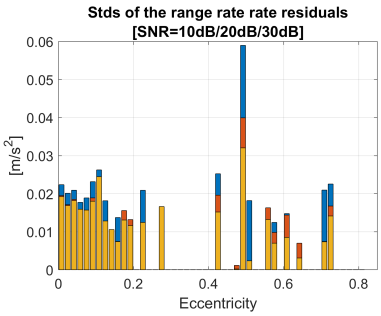

(b) Std distribution over eccentricity

Figure 7. Range rate rate residuals (blue: 10 dB, orange: 20 dB, yellow: 30 dB)

The previous analysis showed that the processing leads to similar performance for all the investigated objects. The number of pulses for the filtering has to be carefully chosen. On the one hand, a too long processing time (>5-10 s) reduces the quality of the range estimate, since the underlying quadratic model is not valid any more. On the other hand, if the number of pulses is too small (<1 s), the initial estimates of the range rate and of the range rate rate may not be accurate enough, yielding ambiguous final estimates.

5. CALIBRATION MEASUREMENTS

The new processing methods for the tracking and the imaging radars were applied to several calibration measurements for which high-resolution ephemerides were available. The first calibration campaign took place in March 2019, when three passes of Stella and three passes of Jason-2 were observed. In January 2021, the ESA satellites Sentinel-3A and 3B were observed two times each. These measurements were used to correct the system bias[1] and demonstrate the performance of the new experimental mode.

[1]Due to the small number of calibration measurements, it was assumed that the systematic errors were identical over the time span 2019-2021, although it turned out that this assumption was not quite true, in particular for the tracking radar.

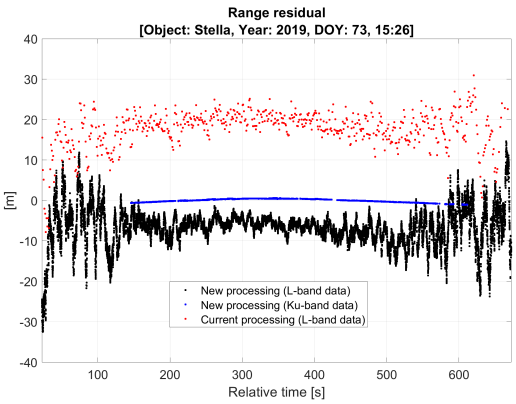

(a) Range residuals

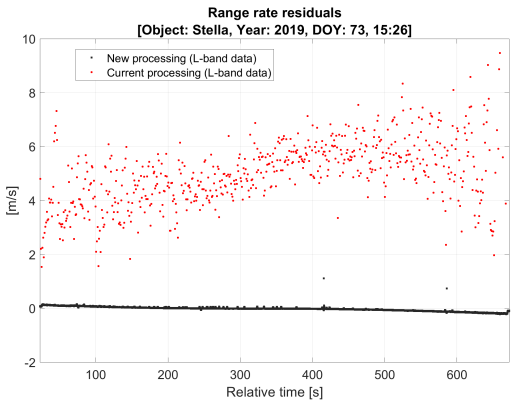

(b) Range rate residuals

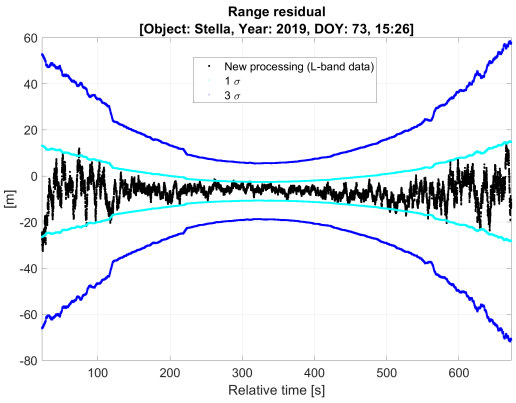

(c) Range residual with corresponding estimation accuracy

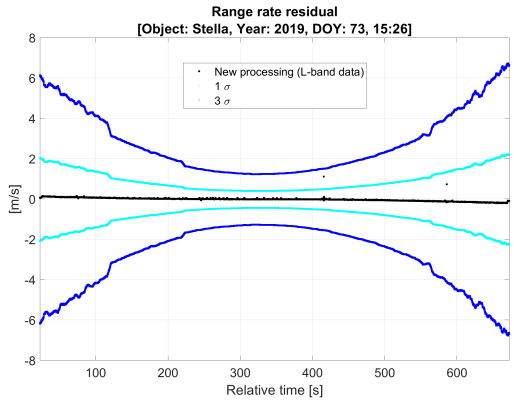

(d) Range rate residual with corresponding estimation accuracy

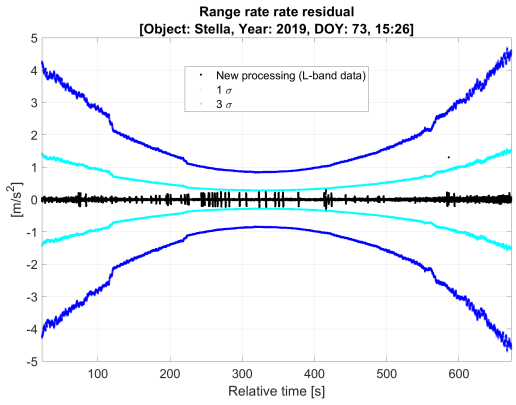

(e) Range rate rate residual with corresponding estimation accuracy

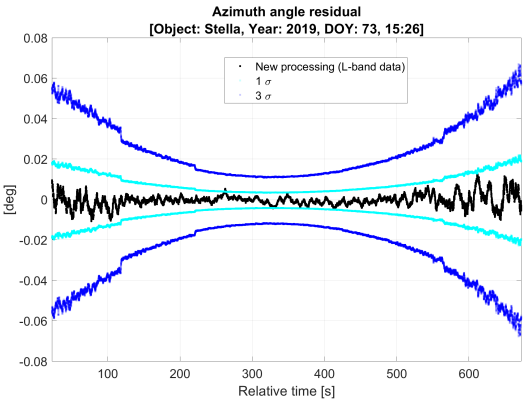

(f) Azimuth angle residual with corresponding estimation accuracy

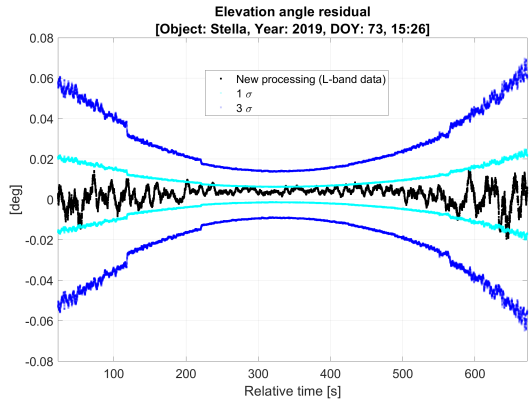

(g) Elevation angle residual with corresponding estimation accuracy

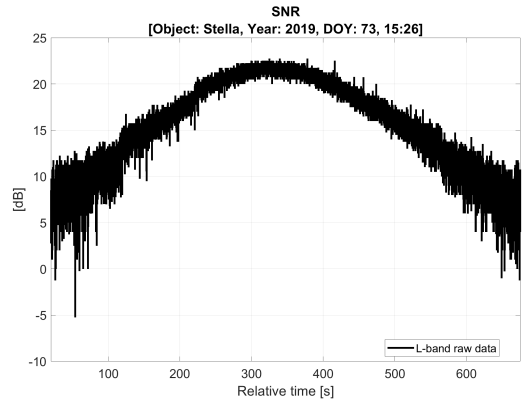

(h) SNR

Figure 8. Stella

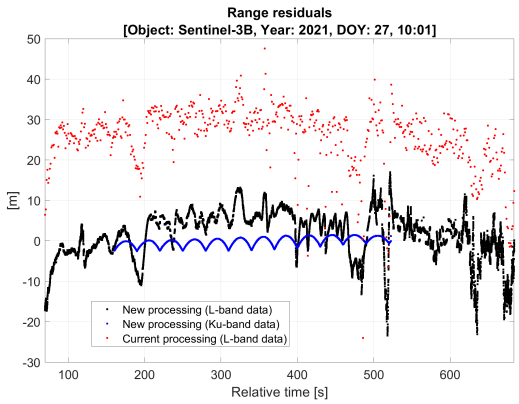

(a) Range residuals

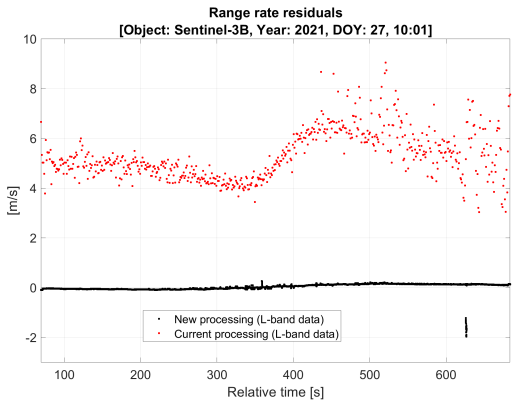

(b) Range rate residuals

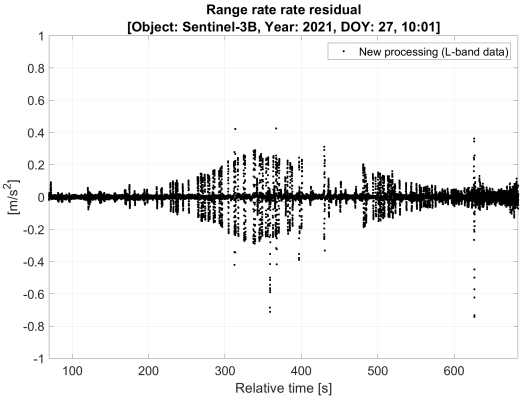

(c) Range rate rate residual

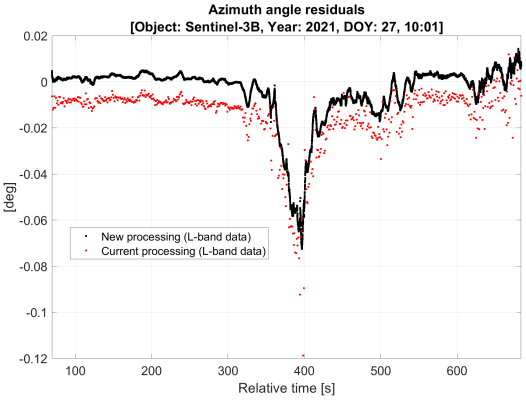

(d) Azimuth angle residuals

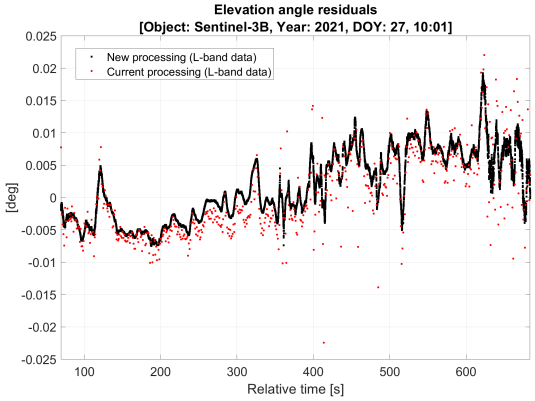

(e) Elevation angle residuals

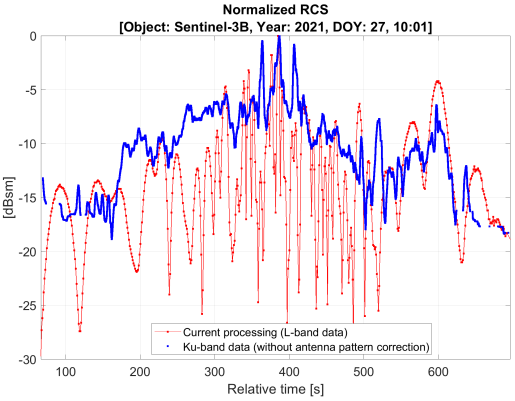

(f) RCS

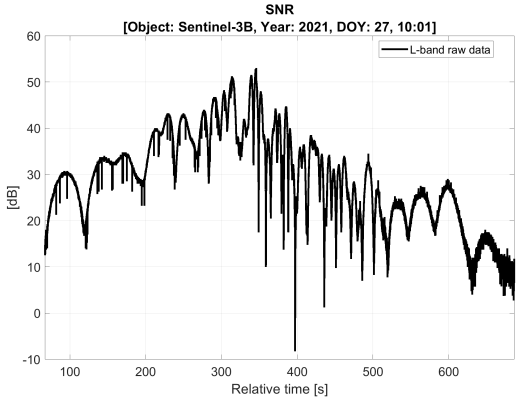

(g) SNR

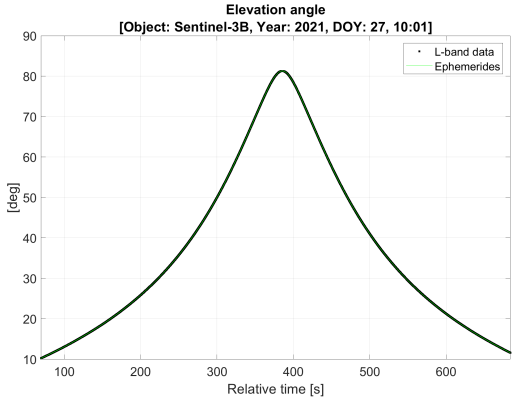

(h) Elevation angle

Figure 9. Sentinel-3B

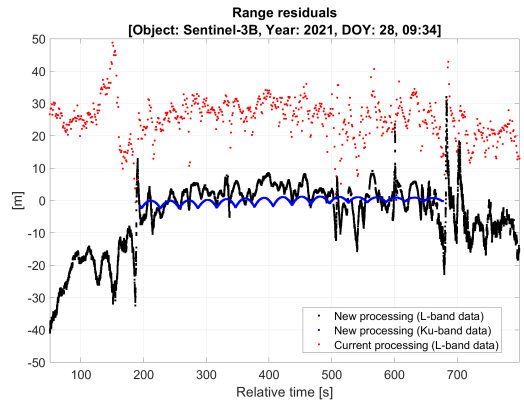

(a) Range residuals

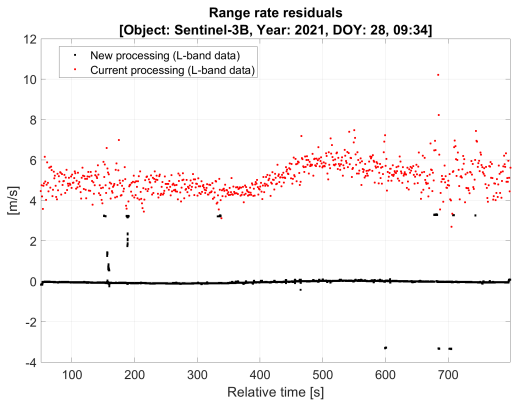

(b) Range rate residuals

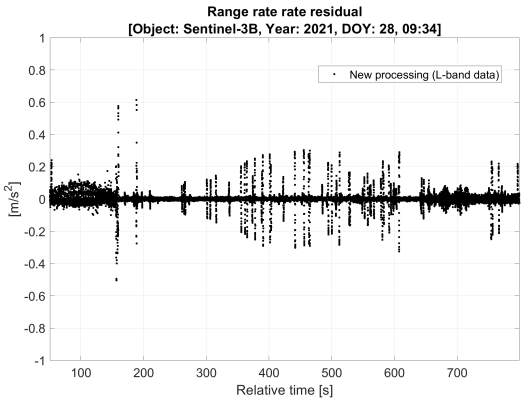

(c) Range rate rate residual

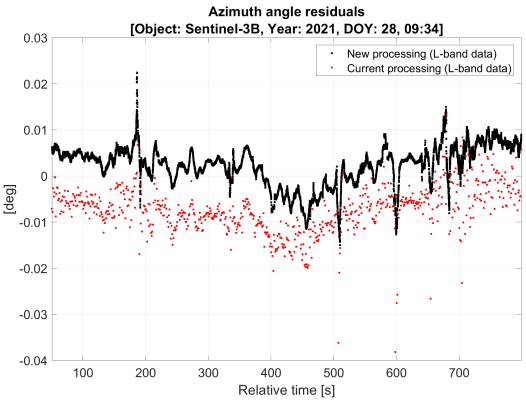

(d) Azimuth angle residuals

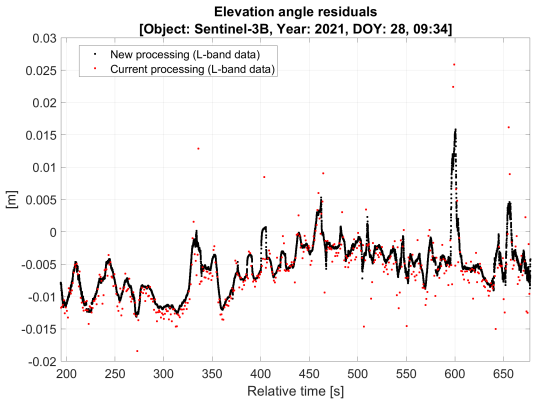

(e) Elevation angle residuals

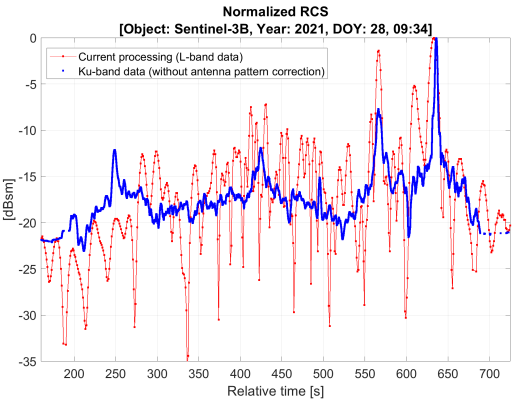

(f) RCS

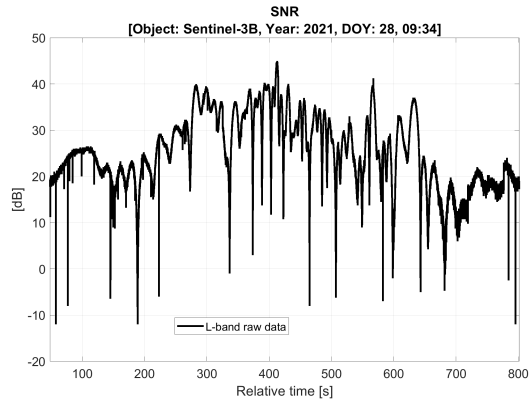

(g) SNR

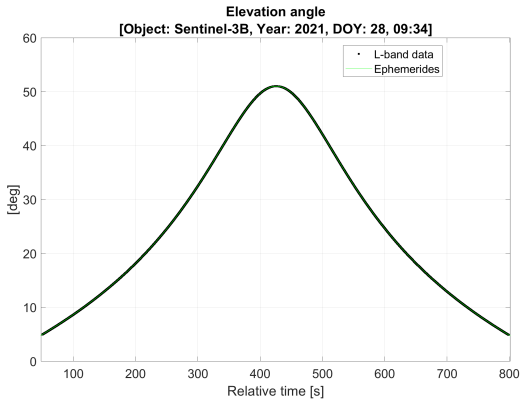

(h) Elevation angle

Figure 10. Sentinel-3B

5.1. Point-like object

Stella was chosen as first calibration object due to its spherical shape of 24 cm diameter. The satellite is equipped with 60 retro-reflectors. This shape offers the advantage that the signal backscattered by Stella is contained in one (or in very few) range cell(s) of a range profile acquired by the imaging radar. Consequently, Stella can be roughly modelled as a point target.

Figure 8 presents the results of the first observation of Stella[2]. The SNR measured by the tracking radar is shown in Figure 8(h). The fast variations are typical for spherical shaped objects with retro-reflectors. The modulation of the SNR according to the range law is clearly visible. The SNR is the highest in the middle of the pass when the range is the smallest and the elevation the highest. Figures 8(c) to 8(g) show the residuals for the range, range rate, range rate rate, and azimuth and elevation angles, respectively, as well as their corresponding estimation accuracy. A very good fit between the measurements and the theoretical boundaries can be observed. The dependency of the estimation accuracy on the SNR can be clearly seen: as the SNR decreases, the variances of the measurements increase.

For all the calibration measurements performed in 2019, a time shift correction had to be applied to the ephemerides. The time shifts, which were different for each performed observation, were estimated to maximize the correlation between the measured parameters and the ephemerides. For the considered Stella observation, a time shift of 0.417 ms was assumed and compensated.

Figure 8(a) compares the range residual of the current processing for the L-band radar (red dots) with the one of the new processing of the L-band data (black dots) and the one of the Ku-band radar (blue dots). As expected, the range can be much more accurately measured by the imaging radar. The reason for the small curvature of the Ku-band radar residual is not clear. It could come from the ephemerides or from an imperfect compensation of the atmospheric effects. Currently, the tropospheric correction is performed according to the Hopfield model with the Saastamoinen zenith range correction [11]. An atmospheric correction based on a numerical integration was also implemented and tested [12]. This method yielded similar results.

Figure 8(b) reveals that the new method is able to determine the range rate more precisely. A small linear trend in the range rate estimate was registered caused by a system drift. A heuristic temperature-dependent phase compensation was developed and applied to the data in a preprocessing step to compensate this drift. This phase correction has to be checked with additional measurements.

[2]In the following, the results of the new processing mode are shown with a revisit rate corresponding to the PRF in order to detect potential outliers. Two successive values are extremely correlated to each other as $N-1$ out of the N pulses used for filtering are equal. The final observation vectors will be decimated to reduce the correlation between subsequent output values.

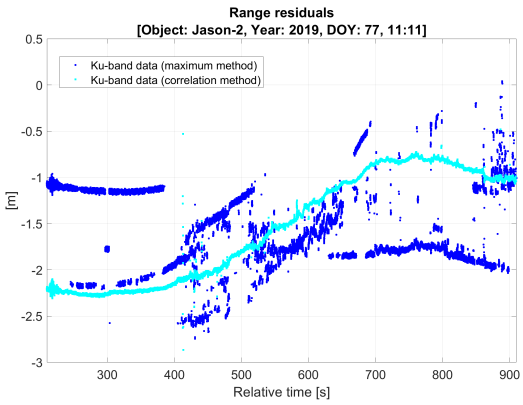

Figure 11. Range residuals computed with two different methods, Ku-band radar

5.2. Complex object

The results of the two observations of Sentinel-3B are presented in Figures 9 and 10. The elevation was over 80 deg for the first observation (Figure 9(h)). In order to continuously track the satellite when the elevation angle is the highest, the antenna has to rotate very fast in azimuth, thus explaining the shape of the azimuth residuals in Figure 9(d). The SNRs (Figures 9(g) and 10(g)) and RCSs (Figures 9(f) and 10(f)) are changing very fast over time and are typical for complex objects. Note that it is possible to measure a second RCS with the TIRA system. It is extracted from the range profiles of the Ku-band radar (see also Section 3.2). These multi-frequency band RCS plots could help better characterizing the space objects. Figures 9(d), 9(e), 10(d), and 10(e) reveal that the angle estimates are slightly improved compared to the current processing. As for the Stella observation, the range rate rate parameter in Figures 9(c) and 10(c) can be accurately captured by the developed processing. The processing is, however, sensitive to strong SNR drops. This effect is visible in the range rate residuals in Figures 9(b) and 10(b). Although the overall estimation performance is much improved compared to the current processing, some range rate outliers and ambiguities occur at time instants corresponding to a SNR fall. The ambiguities for the range rate estimate appear at a multiple of 3.4 m/s. To alleviate this issue, a data selection filter should be implemented as a pre-processing step. Also the range rate unwrapping filter should be improved.

Figures 9(a) and 10(a) confirm that the range of the space object can be measured more accurately by the Ku-band radar. For extended objects such as Sentinel-3A/B, whose dimensions are larger compared to the range resolution of the radar, the reference point scatterer on the object from which the range is evaluated can vary from pulse to pulse. This effect causes a variation of the estimated range within the object dimension. Several methods can be used to extract the range from the range profiles. The simplest one is to consider the range of the strongest scatterer in each range profile. The drawback of this method

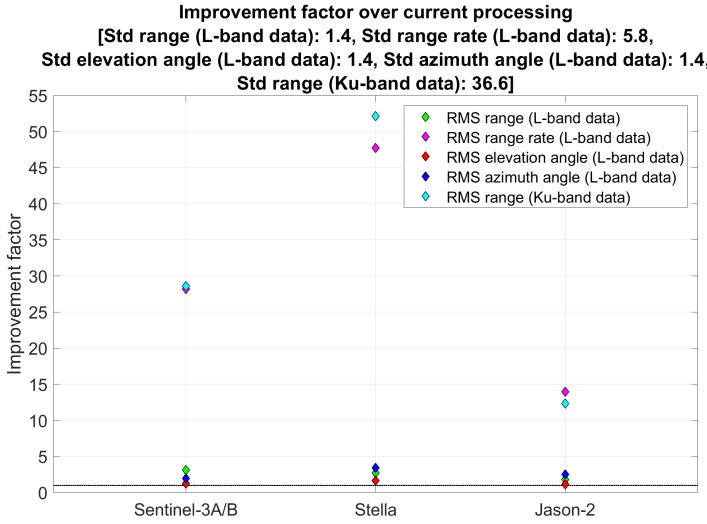

Figure 12. Statistical analysis

is that the estimated range can jump from pulse to pulse, as different point scatterers on the object may reflect the strongest signal. Another method can be applied that exploits the correlation of the range profiles. In this case, the estimated range corresponds to the reflection center. This range also varies over time but more smoothly compared to the other method. Figure 11 illustrates the estimation of the range with these two methods. The method used to estimate the range in Figures 9(a) and 10(a) is the correlation method. The interesting range patterns are similar in both figures. Alternatively, a method could be developed that tracks the center of mass of the satellite over time in order to reduce the variability of the range estimate. This method would require the knowledge of the position of the center of mass of the satellite. This information is usually not available for non-cooperative objects. By exploiting a series of ISAR images computed from the same range profiles from which the range is estimated, the position of the center of mass of the satellite could be determined and its range tracked over time. Such a method would be, however, very time consuming. It is also questionable if the development effort would be worthwhile, since the primary use of this experimental mode is for non-cooperative targets. For those objects, no a-priori knowledge about the object shape and characteristics is available.

5.3. Statistical analysis

The statistics of the residuals based on the std and on the Root Mean Square (RMS) error were examined for the 10 performed calibration measurements. The results are plotted for each satellite in Figure 12. For the estimation accuracy of the azimuth and elevation angles (L-band data) and of the range (L-band data), an improvement for the std of 1.4 could be achieved in comparison to the current processing[3]. A major enhancement for the std is reached for the range rate by a factor of 5.8 (L-band data) and for the range estimated from the Ku-band data (factor 36.6). Note that the latter improvement factor is particularly high for Stella, which can be modelled as a point target. The improvement factors for the RMS are even larger because of the bias present in the current processing method.

6. APPLICATIONS

In addition to delivering observation vectors with improved accuracy to our partners, the developed observation mode can be used for a variety of applications. This section introduces some potential applications.

6.1. Multi-frequency RCS analysis

The radar backscattering is a highly complex process. It depends on several parameters such as the material, orientation and shape of the object, the polarization of the radar waves and the used radar frequency. The relative roughness of the object surface and the relative object size with respect to the wavelength play also a major role. Depending on this relative size, different backscattering regimes occur (Rayleigh, Mie, or optical scattering) [6].

Since the backscattering process is frequency dependent, a multi-frequency RCS analysis has the potential to better characterize the space objects. Figure 13 shows two additional RCS measured in two distinct frequency bands.

[3]This corresponds to the improvement that would have been obtained with a doubling of the transmit power for the current processing.

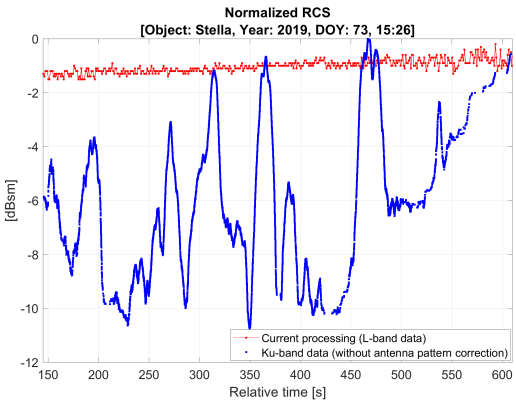

(a) Stella

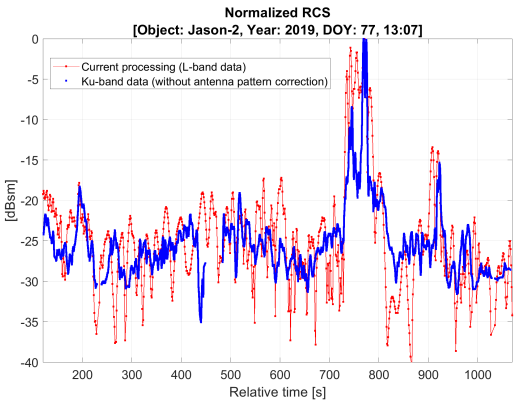

(b) Jason-2

Figure 13. RCS in L-band and Ku-band

While the RCS for large complex objects such as Jason-2 presents some similarities between the L-band and the Ku-band, the backscattering for smaller object such as Stella strongly differs. The dimension of Stella, a 24-cm sphere equipped with retro-reflectors, is similar to the size of the L-band wavelength (22 cm) but is much larger compared to the wavelength of the Ku-band radar (1.8 cm). This explains the difference in the backscattering. A specular reflection mainly occurs in the Ku-band. The oscillations are caused by the relative rotation between the retro-reflectors on Stella and the radar. They could be used to investigate the apparent attitude motion.

The RCS was estimated from the Ku-band data by selecting the parts of the range profiles containing the signal backscattered by the object. Note that there is an ambiguity between the RCS and the SNR measured by the tracking radar. A weak SNR could originate from a low RCS or from a position of the object at the edges of the antenna beam. For this reason, the RCS was estimated without antenna pattern correction (the antenna footprint in the Ku-band is 12 times smaller than the L-band antenna footprint), since the positioning accuracy is too low at low SNR to discriminate between these two cases.

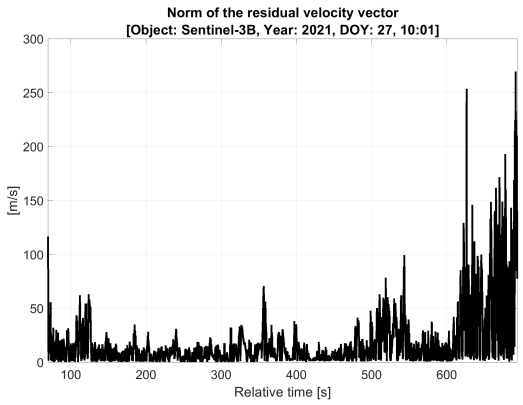

Figure 14. Velocity vector residual (Sentinel-3B)

6.2. Initial orbit determination (IOD)

An interesting application is the IOD of unknown objects, which are not contained in any catalogue. This is e.g. the first step in the development of an autonomous tracking mode for the TIRA system [13]. So far, TIRA uses external sources of information (TLE data) in order to track and observe space objects and cannot follow any target when this information is not available. Also in the context of a BPE (Beam-Park Experiment), the use of IOD techniques to assess the full six Keplerian parameters for each detected object could help better characterizing the space debris population. A comparison of the performance of several IOD techniques for radar systems is investigated in [14].

In order to make full use of the extended observation vectors containing the newly estimated range rate rate, a new IOD technique was developed, which exploits this information in addition to the other radar observables [15]. Knowing this parameter and using conditions that govern the object dynamics, the velocity vector of the space object can be fully determined. Figure 14 presents the norm of the velocity vector residual estimated with this method for the first observation of Sentinel-3B (Figure 9). Only the L-band data were used to compute the initial state vector. The corresponding IOD performance for the velocity vector estimate against the SNR is shown in Figure 15. It was assessed through a Monte-Carlo simulation using the methodology presented in Section 4. A good agreement between the experimental results and the theoretical performance can be observed. In order to avoid saturation issues, limiters attenuate the receive signal so that the lower bound for the estimation accuracy is set by 33 dB. A higher SNR would thus not improve the estimation accuracy. Note that each velocity vector in Figures 14 and 15 was estimated from 5 s of data corresponding to an observation of 0.08% of the full orbit in the case of Sentinel-3B. The influence of a low SNR on the estimation accuracy of the state vector can be observed in Figure 14 for relative times larger than 620 s. [14] examines the performance of this IOD method in more details.

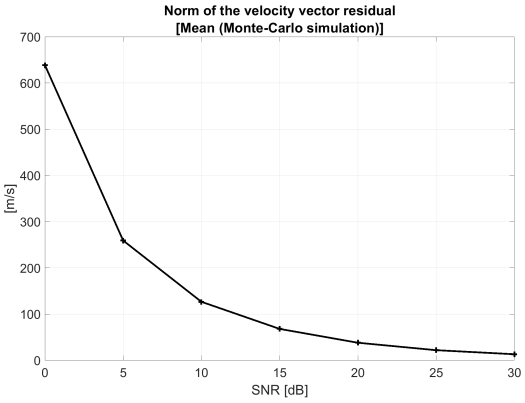

Figure 15. IOD performance (velocity vector)

6.3. Tracking and orbit determination

Another application that could benefit from these improved observation vectors is the tracking and orbit determination of space objects. In [16], the performance of the EKF (Extended Kalman Filter) is assessed according to different input data. For the practical implementation of a tracking filter for a real time operation, the question was raised which kind of input data (raw observation vectors with a high revisit rate or averaged or rather filtered observation vectors with a much lower revisit rate) leads to the best filter convergence and performance. The EKF was modified to take into account the range rate rate information. It was shown that the quality of the input data prevails over the revisit rate up to a certain limit.

Another aspect is the prediction of collision probabilities between space objects. Increasing the quality of the observation vectors may help in the decision making process of a collision avoidance manoeuver.

6.4. Separation of multiple objects

As shown previously, the radar measurement space includes six observables (range, range rate, range rate rate, azimuth angle, elevation angle, and SNR/RCS) at a given epoch. All these parameters can be jointly exploited to discriminate between several space objects that are located simultaneously in the antenna beam. Another benefit of the proposed approach is the improvement of the SNR through the coherent processing over several radar pulses. This allows the detection of weak objects that could not have been detected over one single radar observation. Such a processing could be particularly interesting for LEOP (Launch and Early Orbit Phase) support or for the monitoring of GEO satellites.

Figure 16 shows the detection of four GEO satellites together with their estimated parameters. The same coherent processing was applied to the different receive channels of the tracking radar. The monopulse ratios between the sum and difference beams were computed in order to determine the elevation and transverse angles. By comparing the parameter distributions in the different radar subspaces, the space objects can be discriminated from each other and their parameters can be estimated. All these parameters could be fed into a tracking filter in order to follow their motion over time. Similar ideas were already presented in [17, 18].

7. CONCLUSION AND FUTURE WORK

This paper has introduced a new experimental observation mode for the TIRA system. This mode combines and fuses the information contained in the data acquired by the two radars of the TIRA system. A new processing method was developed for the tracking radar in order to improve the estimation accuracy of the observables and to extract a new parameter, the range rate rate. Due to the larger system bandwidth, the imaging radar has the potential to measure the range of the object more precisely than the tracking radar. A method was developed to determine the absolute range with the imaging radar and to solve the ambiguity between range and range rate intrinsic to the use of linear frequency modulated signals.

An extensive simulation showed that the developed processing could be applied to any space object. A dependency on the orbital parameters could not be noticed. The method was also applied to several measurements for which precise ephemerides were available. An improvement of the estimation accuracy of all the radar observables could be observed. The range rate rate could be robustly estimated with a high accuracy. For extended objects, the estimation accuracy of the range with the imaging radar was smaller than the object size. The range rate was the most challenging parameter because of the low PRF used by radars for space observation and the resulting Doppler ambiguities. Special care was taken to estimate and correct the systematic errors for the different observables and assess their estimation accuracy.

These new generated observation vectors were successfully used in the context of IOD, tracking and object discrimination. In all these cases, an improvement of the achieved results could be observed. This experimental mode presents a high potential for an implementation in a future operational mode, although it still has to be consolidated and robustified against SNR variations. In order to further improve the quality of these filtered observation vectors, a more robust unwrapping filter should be developed for the range rate to solve the Doppler ambiguities. A pre-processing filter suppressing the outliers should be also implemented. The estimation accuracy for complex objects presenting a strong SNR variation should also be improved to better model the data. The heuristic temperature-dependent phase correction should also be confirmed or updated through additional calibration measurements. Finally, a method yielding range estimates with less variability should be developed for the Ku-band radar.

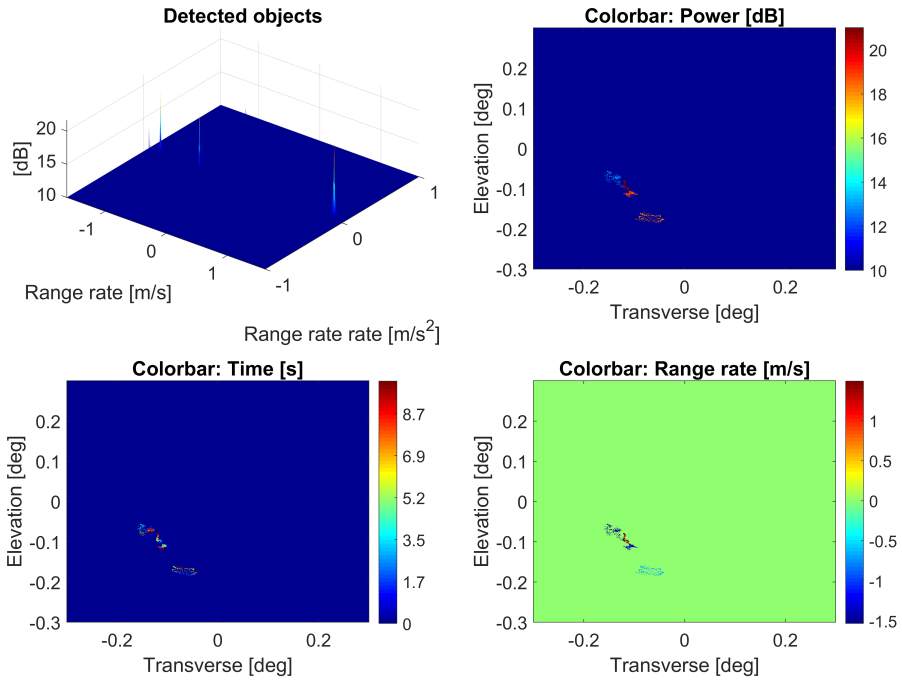

Figure 16. Radar measurement space and space object separation

ACKNOWLEDGMENTS

The authors would like to thank the GSSAC and ESA for providing high-resolution ephemerides for the calibration measurements. This work has been partially funded by DLR (Contract No. D/301/67264737) and by the German MOD (Ministry of Defense).

REFERENCES

1. D. Mehrholz: *Ein Verfolgungs- und Abbildungsradarsystem zur Beobachtung von Weltraumobjekten*, Frequenz, Bd. 50, Ausgabe 7-8:138–146, Juli-August 1996.

2. https://public.ccsds.org/Pubs/503x0b2.pdf.

3. H. Wilden, C. Kirchner, O. Peters, N. Ben Bekhti, A. Brenner, and T. Eversberg: *GESTRA - A phased-array based surveillance and tracking radar for space situational awareness*, IEEE International Symposium on Phased Array Systems and Technology, 2016.

4. H. Wilden, C. Kirchner, O. Peters, N. Ben Bekhti, R. Kohlleppel, A. Brenner, and T. Eversberg: *GESTRA-technology aspects and mode design for space surveillance and tracking*, Proc. 7th European Conference on Space Debris, Darmstadt, Germany, 2017.

5. D. Mehrholz: *Radardatengewinnung und Fehleruebertragung bei der Beobachtung von nichtkooperativen Objekten im erdnahen Weltraum*, PhD, Universitaet der Bundeswehr, 1988.

6. M. Skolnik: *Introduction to Radar Systems*, McGraw-Hill Science/Engineering/Math, 2002.

7. M Soumekh: *Synthetic Aperture Radar Signal Processing with MATLAB Algorithms*, Wiley-Interscience, 1999.

8. D. Cerutti-Maori, I. Sikaneta, and C. Gierull: *Optimum SAR/GMTI processing and its application to the radar satellite RADARSAT-2 for traffic monitoring*, IEEE Transactions on Geoscience and Remote Sensing, 50(10):3868-3881, October 2012.

9. M. Budoni, C. Carloni, D. Cerutti-Maori, L. Fuhrmann, V. Karamanavis, J. Klare, T. Patzelt, and J. Rosebrock: *Tracking radar analyses of low-Earth objects*, Final report, DLR Contract No. D/301/67264737, 2019.

10. M Budoni, C. Carloni, D Cerutti-Maori, I. Maouloud, J. Rosebrock, S. Flegel, and S Lemmens: *Investigation of the radar parameter subspace for different beam-park simulations with the TIRA system*, 71st International Astronautical Congress, 12-14 October 2020.

11. C. Goad and L. Goodman: *A Modified Hopfield Tropospheric Refraction Correction Model*, presented at

the AGU Fall Meeting, San Francisco, California, December 1974.

12. L. Blake: *Ray Height Computation for a Continuous Nonlinear Atmospheric Refractive-Index Profile*, Radio Science, Vol. 3 (New Series), No. 1, January 1968, pp. 85-92.

13. M Budoni, C. Carloni, D Cerutti-Maori, and F. Piergentili: *Autonomous tracking mode with space observation radar: Initial Orbit Determination and Tracking*, ESA NEO and Debris Detection Conference, 2019.

14. M. Budoni, C. Carloni, D. Cerutti-Maori, J. Rosebrock, I. Maouloud, and J. Siminski: *Investigation of different initial orbit determination methods for radar beam park experiments*, Proc. 8th European Conference on Space Debris, Darmstadt, Germany, 2021.

15. M Budoni, C. Carloni, D Cerutti-Maori, I. Maouloud, and J. Rosebrock: *Investigation and comparison of the performance of selected IOD techniques for BPE with the TIRA system*, Intermediate report for WP5300, ESA Contract No. 4000127260/19/D/SR, 2021.

16. C. Carloni, M. Budoni, D. Cerutti-Maori, and J. Rosebrock: *Performance analysis of tracking filters according to input data processing*, Proc. 8th European Conference on Space Debris, Darmstadt, Germany, 2021.

17. L. Leushacke and C. Czeslik: *High doppler resolution monopulse techniques for the radar observation of targets in the geosynchronous ring*, DGON/ITG International Radar Symposium, Vol. I, pp. 457–464, Munich, 1998.

18. T. Patzelt and J. Rosebrock: *Chirp filter bank for selective tracking of space objects on almost identical orbits*, 20th International Radar Symposium, June 2019.